Clustering and precipitation in Al-Mg-Si alloys during linear heating

Zi Yang[1], Igor Erdle[1], Chunhui Liu[2], John Banhart[1]

[1] Helmholtz-Centre Berlin for Materials and Energy, Hahn-Meitner-Platz 1, 14109 Berlin, Germany

[2] State Key Laboratory of High-Performance Complex Manufacturing, Central South University, Changsha 410083, China

Abstract

Differential scanning calorimetry (DSC) is a technique extensively applied to analyse precipitation phenomena in Al-Mg-Si alloys, yet the processes occurring during non-isothermal DSC heating, in particular the formation of clusters in the early stage and their evolution at higher temperatures, remain obscure. Here, we carry out experiments not only to measure heat (via DSC) but also to measure hardness, positron lifetime, electrical resistivity and microstructure of an Al-Mg-Si alloy heated at 3 different rates. Electrical resistivity is measured in-situ, the other properties after interrupting the heating process. It is demonstrated that the precipitation process during heating can be divided into various stages, with transition temperatures depending on the heating rate, but the relative behavior of the various measured quantities are connected in the same way. Quenched-in excess vacancies are found to play an important role in cluster formation at lower temperatures, which explains the seeming peculiarity that linear heating at lower temperatures can lead to stronger clustering than isothermal ageing at a higher temperature. These trends are well simulated using a recently developed precipitation model. New aspects about the evolution of these clusters at higher temperatures are revealed by correlating the different measured properties. The methodology applied here could also be extended to investigating more complex non-isothermal heat treatments.

1 Introduction

Temperature and time are the two key parameters controlling the precipitation processes in age-hardenable alloys including Al-Mg-Si alloys, where the primary alloying elements Mg and Si may form various metastable or stable precipitates of different compositions, structures, and strengthening capabilities according to the applied ageing conditions. Depending on whether temperature changes during the process, ageing can be called isothermal or non-isothermal. Isothermal ageing is well investigated and many studies have contributed to elucidating the microstructure/property evolutions during ageing at various temperatures experimentally and with models [1-11]. In contrast, non-isothermal ageing is more complex and less frequently investigated although this type is also commonly seen in realistic industrial processing, e.g. in the heat-affected zone of welding [12] or during heating and cooling stages of pre-ageing [13]. Given the fact that precipitation in Al-Mg-Si alloys is sensitive to the solute clusters formed at low temperatures [14, 15], temperature variation might play a more complex role than simply altering the kinetics in an Arrhenius-like fashion. The microstructural evolution during non-isothermal processes remains to be better characterised and modelled, especially when both clusters and precipitates are involved.

Among the vast number of possible non-isothermal temperature profiles, the most simple form stands out, namely linear heating, where the temperature increases at a constant rate. Such a temperature profile is often seen in differential scanning calorimetry (DSC), a widely used method for analysing precipitation in aluminium alloys [16] and other materials. It involves measuring the thermal effects caused by precipitation reactions and has been typically applied, i) to reveal the precipitation sequence during ageing [17, 18], or ii) to study the influence of other pre-treatments by comparing the DSC traces before and after [19-25]. For the interpretation of DSC data it is necessary to have a fundamental understanding of the peaks appearing in the DSC trace and correlate them with microstructural changes. DSC provides one aspect, namely the associated thermal effect, but it is often insufficient, especially

when multiple reactions occur simultaneously and a complex signal is obtained. By applying DSC during cooling/quenching one avoids many of these problems [26, 27] but still, most current DSC measurements are performed during heating, whereas the majority of studies rests on isothermal ageing treatments and measurements of properties such as hardness, strength, electrical resistivity and the characterisation of microstructure. Therefore, there is a gap to bridge between DSC results and the bulk of data from isothermal ageing. It has been attempted to carry out DSC at constant temperature, but the difficulties are very large [21, 28, 29]. Another strategy is to characterise other quantities non-isothermally, i.e. during linear heating: For example, hardness measurements on samples quenched after linear heating provide a direct comparison to DSC [30-32]. Electron microscopy and atom probe tomography have been applied to identify the phases formed during linear heating [17, 18, 31]. Among them, the earliest precipitation phenomenon —"solute clustering"— remains particularly elusive. Atom probe tomography does show the existence of clusters and provides some important information such as the sizes and chemistry of the clusters that are hard to be assessed from other methods, but the data in the literature are not always consistent [33]. Therefore, indirect methods such as resistivity and hardness are still important to study clusters. Excess vacancies are known to be crucial for clustering at low temperatures, and recently the current authors have found that the role of excess vacancy is different at various isothermal ageing temperatures due to a competition between vacancy annihilation and cluster formation kinetics [34]. But how does clustering proceed during linear heating, what is the influence of heating rate, and what about the further evolution at higher temperatures?

It is the aim of this work to carry on such work more systematically by combining various quantities measured at different heating rates. DSC device was primarily used in earlier studies to perform linear heating, and due to the sample size and geometry many other characterisation techniques were hard to be applied. Here we constructed an apparatus to carry out linear heating on flat samples, the geometry of which can be varying, thus enabling us to conduct more characterisations of the material. Ideally,

properties are measured in-situ during heating and only where this is not possible, we need to interrupt linear heating by quenching and measure properties ex-situ. We carried out in situ resistivity measurements and ex-situ positron annihilation lifetime spectroscopy (PALS), hardness testing and transmission electron microscopy (TEM) after linear heating in addition to the conventionally applied DSC to reveal more aspects of the precipitation phenomena in Al-Mg-Si alloys during linear heating at 3 different rates, especially the formation of solute clusters in the early stage as well as their evolution at higher temperature.

2 Experimental

2.1. Material and heat treatment

Commercial aluminium alloy 6014 was provided by Novelis Switzerland. It contains 0.65% Mg, 0.60% Si, 0.18% Fe, 0.08% Mn, 0.12% Cu (all in wt.%) in addition to Al. Samples were prepared in various geometries (Fig. 1a) before solution heat treatment was conducted at 540 °C for 1 h in an air circulation furnace or in a vertical quenching furnace in an argon-atmosphere. After quenching in ice-water, samples were transferred immediately into the heating device (schematic in Fig. 1b and photos in Fig. S1) and ageing was carried out. Exposure of the samples at room temperature (RT, ~20 °C) before ageing was minimised (<1 min). More information of the heating device can be found in the supplement S1. Samples were then either linearly heated from RT to a target temperature or isothermally held at an elevated temperature (with the heating device pre-heated to the desired temperature). Three different heating rates, namely 3 $K \cdot min^{-1}$, 10 $K \cdot min^{-1}$, and 50 $K \cdot min^{-1}$, were employed in linear heating. The temperature of the sample during linear heating was monitored by a thermocouple inserted through the hole in the heating plate and touching the sample surface (Fig. 1b). Once the target temperature was reached, samples were removed immediately from the heating plate and quenched in ice-water, after which the ex-situ characterisations were carried out. Typical measured

temperature curves are given in Fig. 1c. A very small overshoot is seen at the beginning but the influence of such low-temperature inaccuracies is negligible.

2.2. Methods

Brinell hardness measurements were carried out with a Qness M60 tester applying 10 kgf load and a 1 mm diameter indenter on platelet-shaped samples (10×10×1 mm^3). An average hardness and standard deviation were calculated from 8 indentations on each sample.

DSC was measured on disks of 4.8 mm diameter and 1 mm thickness using a Netzsch DSC 204F1 Phoenix unit at 3 different heating rates. Measurements started from 0 °C to 400 °C for the two lower heating rates and from −70 °C for 50 $K \cdot min^{-1}$. These low starting temperatures were chosen to be able to separate the initial signal instability from the first sample-related peak, but they have no obvious impact on the measured signal compared with those started from room temperature (see supplement Fig. S2). Pure aluminium of similar mass as the alloy sample was used as the reference. The baseline correction is done using the double-ramp method described elsewhere [20, 22].

Electrical resistivity measurements were performed on meander-shaped samples (Fig. 1a, thickness 0.3 mm) using the four-point probe method and a constant current of 100 mA. This sample shape ensures a maximum current path while keeping the sample area small and was prepared by laser-beam cutting. The voltage and the temperature of the sample were both measured in-situ during linear heating. To obtain the resistivity change caused by precipitation phenomena only, two corrections were performed. In the first, the electrical resistivity was normalised assuming a constant resistivity of the as-quenched sample at 20 °C (Eq. (1)), which is 3911 nΩ cm according to our previous work [20]. The advantage over using nominal geometry values in the calculation (Eq. (S1)) is that the geometry variations between different samples can be ignored and thus results are more comparable (supplement Fig. S3). In the second, the phonon contribution to the electrical resistivity caused by an increasing

temperature was subtracted. Resistivity measurement during reheating, where precipitation is negligible, revealed that such contribution is linearly related to temperature from 20 °C to ~310 °C with a temperature coefficient $\rho' = 11.27$ nΩ cm K^{-1} (supplement Fig. S3). Finally, the resistivity at 20 °C was used as a reference state to calculate the resistivity change caused by precipitation during linear heating using Eq. (2).

$$\rho = \frac{U}{U_{\mathrm{AQ}(20\,^{\circ}\mathrm{C})}} \cdot \rho_{\mathrm{AQ}}(20\,^{\circ}\mathrm{C}) \tag{1}$$

$$\Delta\rho = \rho - \rho'(T - 20) - \rho_{\mathrm{AQ}}(20\,^{\circ}\mathrm{C}) \tag{2}$$

Positron annihilation lifetime spectroscopy was conducted on a fast-fast coincidence spectrometer [35]. This technique makes use of the unique sensitivity of positron lifetime to the local electron density, which is determined by the host matrix and the various defects contained, each having a characteristic positron lifetime. In the alloy system studied and for the treatments applied, positrons annihilate primarily in vacancies, clusters/precipitates, and the Al lattice. The so-called one-component positron lifetime τ_{1C}, which approximates the average positron lifetime of all annihilation events, was evaluated in this study to reveal the relative evolution of the defects. A ^{22}Na isotope of 30μCi activity was used as the positron source, sandwiched by a pair of identically processed square samples (10×10×1 mm^3) during the measurement. The count rate of the spectrometer was ~700 s^{-1}. Software LT9 was used to analyse the positron lifetime spectra collected at RT after linear heating treatment to determine τ_{1C} (supplement S4).

Bright-field transmission electron microscopy (TEM) was carried out using a Thermo Fisher Talos™ F200X field-emission scanning TEM (STEM) operated at 200 kV. The high-angle annular dark-field STEM (HAADF-STEM) mode generating atomic-number (Z) contrast was adopted to image typical precipitates at atomic resolution and to provide structural details. Thin foils for TEM were prepared

by mechanical polishing 3 mm diameter discs to a thickness of ~100 µm followed by twin-jet electro-polishing at 18 V in an electrolyte with 30% nitric acid and 70% methanol cooled to −25 °C.

3 Results

3.1. Evolution of properties during linear heating at various rates

3.1.1. 3 K·min^{-1}

An overview of the various properties as they evolve during linear heating at 3 K·min^{-1} is presented in Fig. 2a. Various exothermic peaks (*a*–*c*) are observed in the DSC trace, which divide the graph into various stages. The first exothermic peak occurs at ~60 °C, characterised by a monotonic hardness increase from ~44 HBW to ~60 HBW, with the fastest change in the middle of the peak. Electrical resistivity first increases in this stage and peaks at ~80 °C after which it decreases slowly. One-component positron lifetime τ_{1C} decreases sharply in the initial period of the stage and later changes marginally. The second stage involves only a small heat effect as revealed by the DSC trace. This small exothermic signal is considered real, i.e. not the residual of an imperfect baseline correction, because other properties are slowly evolving as well: Hardness increases, electrical resistivity decreases, and τ_{1C} decreases. This is then followed by a strong exotherm (peaking at 232 °C) in the next stage of DSC trace, where the hardness reaches its maximum (~100 HBW) and resistivity drops markedly. Positron lifetime τ_{1C} first drops in the first half of the peak and re-increases in the second. The next exotherm is accompanied by a loss of hardness, a further reduction in electrical resistivity, and an increase of τ_{1C}. The final stage features an endotherm and softening of the alloy.

3.1.2. 10 K·min^{-1}

The evolution of properties during heating at 10 K·min^{-1} follows a similar trend as at 3 K·min^{-1}, see Fig. 2b. The major differences are that the DSC and hardness peaks appear at higher temperatures and the corresponding property changes are lower. For example, the exothermic peaks *a*–*c* have shifted to

80 °C, 246 °C, and 298 °C, respectively, and the hardness level after the peak *a* is now ~55 HBW, lower than 60 HBW for 3 K·min^{-1}. Moreover, the electrical resistivity increase in stage 1 as well as its decrease in stage 3 and 4 are also lower. In contrast to other observables, the evolution of τ_{1C} at 10 K·min^{-1} appears very similar to 3 K·min^{-1}, i.e. τ_{1C} drops to a plateau (~221 ps) after heating to 60 °C and later drops to a minimum at ~220 °C before it eventually increases again.

3.1.3. 50 K·min^{-1}

DSC peaks at 50 K·min^{-1} are further delayed to higher temperatures compared with 3 K·min^{-1} and 10 K·min^{-1}, see Fig. 2c. In particular, there is an endothermic trough *d* in stage 2, which is not seen in the previous two graphs. The hardness and electrical resistivity increase in stage 1 are further lowered, and so is the hardness at peak age in stage 3. The electrical resistivity decrease in stage 2 is more pronounced, albeit a larger fluctuation in resistivity data. In analogy to 3 K·min^{-1} and 10 K·min^{-1}, τ_{1C} drops sharply after heating to 60 °C. The minimum of τ_{1C} is found around 220 °C, but it corresponds now to stage 2, while in stage 3 τ_{1C} increases markedly.

3.2. Microstructure of peak-aged alloy (linearly heated)

STEM was applied to investigate the microstructure of the samples aged to maximum hardness at various heating rates in Fig. 2, i.e. 240 °C at 3 K·min^{-1} (sample A), 260 °C at 10 K·min^{-1} (sample B), and 280 °C at 50 K·min^{-1} (sample C), respectively. Fig. 3 demonstrates the typical microstructure imaged from the $\langle 100 \rangle_{Al}$ direction. Bright-field (BF) images (Figs. 3a–c) reveal a dense distribution of needle-shaped precipitates oriented along the $\langle 100 \rangle_{Al}$ directions in all three samples. The structure of the needle precipitates was further investigated at atomic resolution in the high-angle annular dark field (HAADF) imaging mode. A representative needle cross section observed throughout all three samples is presented in Fig. 3d. From the image the following orientation relationship between the precipitate (denoted as 'ppt') and the Al matrix can be noted: $[100]_{ppt} \parallel [\bar{3}\bar{2}0]_{Al}$ and $[001]_{ppt} \parallel$

$[\bar{1}30]_{Al}$. Such relationship is known to be characteristic for the β″ phase in the current alloy system [36]. Using the Al lattice parameter for calibration of drift distortion, we can measure the lattice parameters ($a = 1.536$ nm, $c = 0.648$ nm) of the precipitates according to the single cells marked on the image, which are also very close to that of the β″ phase reported in the literature ($a = 1.516$ nm, $c = 0.674$ nm) [36]. This phase was also found dominant in the microstructure of the current alloy isothermally aged to the peak hardness [8]. The length of the precipitate was measured by the strain contrast shown along the needle. A statistical evaluation of the precipitate length based on ~150 precipitates is presented in Fig. 3e. While only a small difference is observed between sample A and B, a notable shift of the distribution to a larger length is seen for sample C. Therefore, the precipitate type is the same (β″) for peak-aged samples heated at various rates, but longer precipitates are formed at higher heating rates.

3.3. Comparison of linear heating and isothermal ageing for equal times

Isothermal ageing was conducted for the same time as linear heating presented in Fig. 2 and the hardnesses obtained from both approaches are compared in Fig. 4. The isothermal ageing time t at temperature T is given by $t = \frac{T-20°C}{\phi}$, with ϕ the heating rate for the corresponding linear heating to end temperature T. Therefore, for any pair of samples (and hardness results) compared, the temperature during isothermal ageing is always higher than linear heating until the end of ageing. However, this does not guarantee a higher hardness for isothermal ageing than for linear heating: For each heating rate series, four temperature regimes can be discerned from the relative height of the hardness values by the two ageing approaches: In the lowest temperature regime, isothermal ageing results in stronger hardening (I). As the temperature increases, linear heating to higher temperature continuously increases the hardness, while the hardness obtained through isothermal ageing remains constant or even slightly decreases. As a result, a higher hardness is achieved by linear heating (II). Further increasing ageing temperature (and time) in linear heating hardens the alloy moderately, but a marked

rise in isothermal hardening is seen that eventually exceeds hardening during linear heating (III). The hardening caused by isothermal ageing at even higher temperatures (IV) falls below that of linear heating again. These general observations are found for all heating rate series, just the transitions between various regimes occur at higher temperatures as the heating rate increases.

4 Discussion

Precipitation phenomena during linear heating are complex since both the thermodynamic driving force, i.e. supersaturation of solute atoms, as well as kinetic factors such as solute diffusion coefficient and excess vacancy annihilation depend on the current temperature. Another complexity for Al-Mg-Si alloys is that the clusters formed at low temperature are well-known to have a great impact on precipitation at higher temperature. With the aid of the heating device constructed, we have successfully characterised linear heating using methods that have not been applied to this process before, such as in-situ electrical resistivity measurement and positron lifetime. The combined measurements reveal complex changes in various stages, but a closer inspection reveals that they are well correlated. Using this multi-method approach, we are able to reveal some aspects that have not been noted before, which will be discussed in detail next.

4.1. General discussion of precipitation stages during linear heating

The general course of the DSC trace is similar to those previously presented in the literature [17, 18]. The precipitation sequence generally proposed is: supersaturated solid solution→ solute clusters→ GP zones→ β″→ β′→ β (with variations, see Ref. [15]) and can be used to explain the stages observed in Fig. 2: Solute cluster formation corresponds to the peak *a* in the first stage. Within this stage, hardness increases monotonically, but the electrical resistivity experiences a rise first and a slight drop after. This 'anomalous' resistivity increase has been said to be caused by the formation of solute clusters that scatter the conduction electrons most at a critical size [37]. Such critical size was revealed by X-ray small-angle scattering to be ~1 nm in Al-Zn alloys [38], but the corresponding value for Al-Mg-Si is

unknown. Nevertheless, the decrease of the resistivity implies that clusters start to coarsen within the first peak. At the end of this stage the positron lifetime τ_{1C} has reached a level around 220 ps, which is close to the typical lifetime for clusters (~215 ps), suggesting that the number of clusters is close to a value where positron trapping is saturated. For 50 K·min^{-1} (Fig. 2c), positron lifetime has decreased markedly upon reaching 60 °C, whereas DSC shows only a small signal. This can be explained by a high sensitivity of positron lifetime even to small solute clusters. Moreover, the loss of excess vacancies also contributes to this decrease.

Formation of β″ phase explains the second exothermic DSC peak *b* in stage 3. This is confirmed by a large number of β″ precipitates observed in the microstructure within this stage (Fig. 3). Many studies [39-41] have reported that β″ is the most efficient strengthening phase in this alloy, which is in accordance with our observation that such microstructure is correlated with the hardening maximum. A marked decrease in electrical resistivity is associated with the formation of this phase, in line with previous studies [5, 42]. Stage 4 (peak *c*) is ascribed to the β′ phase. The corresponding changes of the properties are monotonic, i.e. electrical resistivity further decreases, hardness drops, and positron lifetime increases to a very high value. Such an increase in τ_{1C} has been observed in isothermal artificial ageing experiments and has been explained by the additional open volume created when full coherency is lost [43-45].

The heating-rate-dependent endothermic trough *d* (Fig. 2c) has not been reported previously. The decreases in electrical resistivity and τ_{1C} as well as a very slight reversion of hardness indicate that this trough is associated with the dissolution of previously formed clusters. However, it is unusual that this dissolution does not show in the traces of 3 K·min^{-1} and 10 K·min^{-1} since a stronger cluster formation is observed there. Therefore, either 1) clusters formed at lower heating rates are more stable and do not dissolve upon heating, or 2) cluster dissolution does occur for other heating rates but is obscured by a stronger exothermic signal because DSC detects only the total of all reactions. The first

explanation is deemed not convincing since natural ageing clusters, which can be considered as formed during extremely slow heating, are actually prone to dissolution during heating, see supplemental Fig. S5. Thus, this strongly suggests that the endothermic signal of cluster dissolution is masked by an exotherm. Such compensation is not likely to occur in stage 2 since other observables are slowly evolving just as the DSC signal and there is no such compensation effect there. If another precipitation reaction occurred one would expect larger changes of properties such as electrical resistivity. Therefore, we suggest that cluster dissolution actually happens in stage 3 and causes the double-peak structure of peak *b*, as will be analysed next.

The double-peak *b* was first reported by Dutta et al. [17], who assumed that it is the superposition of two exothermic sub-peaks, the first assigned to GP-zones and the second caused by β″ formation. Here, we observe that the heating rate plays a crucial role for the appearance of the double-peak structure, just like the endothermic trough *d*, but with an opposite influence. A lower heating rate is associated with a more pronounced double peak and the disappearance of the endothermic signal. Thus, we propose that the dissolution peak has just merged into the β″ peak and is not observed clearly. To demonstrate that such superposition is able to create the observed experimental curves, we used both a positive and a negative Gaussian to fit the DSC trace measured at 3 $K \cdot min^{-1}$ in the relevant temperature range (Fig. 5a). The choice of Gaussians is not based on physical reasons but rather has been empirically found to represent DSC data very well in Al alloys [19, 46, 47], but also in non-metallic systems [48, 49]. Indeed, the experimental curve in Fig. 5a is well reproduced although the match seems not perfect, possibly because the true peak profile is not totally symmetric as suggested by the use of Gaussian functions (for example the dissolution trough *d* in Fig. 2c appears to be in two steps). Adding correction terms to Gaussian functions has been proposed but introduces too many parameters [50] so that we refrain from applying them.

Further indirect evidences supporting our proposal are revealed by positron lifetimes and electrical resistivities. A decrease of positron lifetime τ_{1C}, which occurs at the dissolution peak for 50 K·min^{-1}, is also found at the suspected dissolution positions for 3 K·min^{-1} and 10 K·min^{-1}. This decrease τ_{1C} implies that a lifetime component longer than that of the pure matrix (typical lifetime ≤ 160 ps) is reduced. Elimination of vacancies (typically ~245 ps) is not likely at this stage so that dissolution of clusters is the most plausible explanation. Since cluster formation has caused the anomalous resistivity increase, the dissolution of clusters would diminish this effect, resulting in an additional resistivity loss on top of that caused by precipitation. This is nicely seen when the electrical resistivity is plotted as a function of DSC integral for the peak (Fig. 5b). Data there are taken from a range delimited by the half-maxima of the peaks *b* in Fig. 2, as shown by purple arrows. It is demonstrated that wherever a double-peak is obvious, i.e. at 3 K·min^{-1} and 10 K·min^{-1}, the decrease of resistivity as a function of the DSC integral features two stages (both approximately linear), and the rate of decrease is higher in the first stage than in the second, which is well explained with the dissolution of clusters.

In summary, the experimental data obtained through various methods can be well correlated and explains the stages observed during linear heating. Still, we cannot rule out the possibility of GP-zone formation, which could be the reason for the slowly evolving properties (DSC, hardness, resistivity) in stage 2. However, we proposed a new explanation for the structure of the β″ peak in DSC trace, namely a cluster dissolution trough superposed on it. This information is not readily accessible if no other characterisations are performed and data compared, thus pointing at the complexity of DSC trace and the need for using other observables for the interpretation.

4.2. Cluster formation during linear heating

4.2.1. Influence of the heating rate

As the earliest stage of phase decomposition, cluster formation is of particular interest. As the heating rate increases, apart from an elevated cluster peak temperature, an overall weaker clustering is noticed.

This can be seen in the lower total exothermic energy (DSC integral) after stage 1, a lower achieved hardness plateau level, and a lower resistivity maximum in stage 1 (Fig. 2). Although a higher heating rate is associated with a shorter ageing time, the weaker clustering cannot be explained by ageing time only, because the temperature reached in stage 1 is also higher, i.e. faster kinetics are expected. Thus we explain it from another viewpoint, namely that of excess vacancies. We have recently discussed the role of excess vacancies during ageing at different temperatures, and successfully simulated the experimental characteristics during isothermal ageing at various temperatures and also linear heating at one heating rate by considering the excess vacancy annihilation in a precipitation model [34]. Now we use this model and parameters [51] and apply it to the three heating rates here. Fig. 6 shows the comparison of the DSC clustering peaks from the experiments and the simulations, where it is seen that the main features of the experimental DSC peaks are very well reproduced by the simulations, namely the peak shift to higher temperature, the reduction of both peak height and the integrated peak area with increasing heating rate. The interpretation is that the cluster peak seen by DSC is essentially governed by diffusion processes involving quenched-in excess vacancies, and the gradual removal of excess vacancies results in the end of clustering. In comparison with the initial (as-quenched) vacancy concentration, the equilibrium vacancy concentrations at different end temperatures for various heating rates are all very small and thus the loss of excess vacancies is roughly the same in all three heating conditions. Hence, we can simplify the scenario of clustering during linear heating as the work (transporting solutes) done by all the excess vacancies on the way eventually to sinks, i.e. it is a race between cluster formation and vacancy loss. Excess vacancies are more prone to loss than assisting solute diffusion at higher temperatures than at lower temperatures [34], therefore can cause a weaker clustering observed here for faster heating due to a higher peak temperature.

4.2.2. Hardening mechanisms

Fig. 7a depicts the relationship between hardness changes and the DSC integral, where we notice a clear linearity for the cluster formation stage (Fig. 7b). Data in Fig. 7b is extended to stage 2 and beyond in Fig. 2 (excluding the dissolution trough) and include also the linear heating of a naturally aged condition (natural ageing for 1 h, for detailed DSC and hardness data see supplement Fig. S5). If we assume that the DSC integral Q_{int} is proportional to the extent of clustering (clustered solute fraction α), we obtain a linear cluster hardening mechanism – $\Delta\mathcal{H} \propto \alpha$ – which is in accordance with the model predictions by Starink et al. [52] based on the short-range order strengthening mechanism. This observation is remarkable, particularly because this linearity is found for all heating rates applied and is also independent of the pre-treatment before the linear heating. This implies that this relationship is generally applicable to any temperature profile as long as only clusters are formed.

For the same heat produced, hardening caused by precipitates in underaged and peak-aged states is much stronger and a square root relationship is found to approximate the hardness increase as a function of DSC heat integral (green shaded curve in Fig. 7a). In analogy to cluster hardening, if we assume that the precipitated solute fraction α is proportional to the DSC integral (with different pre-factors), and that the microstructures in the peak-aged state contain only precipitates, i.e. cluster dissolution is finished, a simple square root hardening effect for precipitates is obtained, i.e. $\Delta\mathcal{H} \propto \sqrt{\alpha}$. Esmaeili et al. modelled such relationship in the underaged and peak-aged microstructure using the 'strong obstacle' model for the precipitate shearing [11].

4.2.3. Influence of clustering on the precipitation at higher temperatures

Since in the current alloy the clusters formed at low temperatures have to dissolve upon heating (Sec. 4.1), the precipitation process at higher temperatures will be delayed. Pogatscher et al. have demonstrated this effect by starting heating in a DSC experiment from a temperature high enough to skip the range of cluster formation, and this shifts the precipitation peak to lower temperatures [53].

Moreover, they showed that this shift is more pronounced as the heating rate decreases [53]. Since lower heating rate induces more clusters, this stronger delaying effect is well expected. However, despite of this, a much higher peak-age hardness is still obtained at lower heating rate, which requires a further explanation, and we attribute the effect to following reasons.

First, the total heat production for the peak-aged state is much higher for a lower heating rate as demonstrated in Fig. 7a. This indicates that the total precipitated solute fraction is higher for lower temperature, which is likely to be a result of the higher solute supersaturation at lower ageing temperatures. Moreover, although the precipitates are of same type in peak-aged alloys, the size of precipitates is on average lower for lower heating rates (Fig. 3). This results in a lower inter-particle spacing (higher density) and elevates the stress needed to activate the Orowan mechanism and thus overageing. The reason for a higher density might arise from an overall lower ageing temperature or from the nucleation effect of the undissolved clusters. It has been demonstrated that dissolution is incomplete even after reversion at 250 °C [24]. Undissolved clusters might be of the correct composition to make them nuclei for further precipitation so that they do not dissolve but grow [25, 54]. This positive effect of clusters is generally observed when performing artificial ageing of naturally pre-aged samples at >210 °C [5], which appears to be the temperature range of our current concern.

4.3. Comparison between linear heating and isothermal ageing

Fig. 6 demonstrates that linear heating and isothermal ageing at the end temperature of linear heating for the same time as linear heating define four regimes in the temperature range covered. In regime I and III, isothermal ageing results in higher strengthening, which is the behaviour expected from the reasoning that at a higher temperature, a thermally activated process leads to faster kinetics. Regime IV shows that at very high temperatures isothermal ageing leads to lower strength, which is also understandable, since overageing sets in for this time and temperature and softens the alloy. What seems at first counterintuitive is regime II, where a longer time at higher temperature leads to lower

strengthening in the under-aged state. This phenomenon is not just shown in current alloy, which is slightly richer in Mg, but also in another Si-richer alloy (Supplement S6), thus appears universal. It can be explained by analyzing the role of quenched-in excess vacancies at different temperatures as already done in Sec. 4.2.1, i.e., excess vacancies cause less clustering at higher temperature than at lower temperature. To demonstrate this, we apply the same model used for calculating Fig. 6b [34]. The model is especially suitable to treat cluster hardening since it assumes a linear relationship between the clustered solute fraction (α) and hardening (strengthening), which has been shown in Fig. 7b to be valid here. Fig. 8 shows that the general features including regime I–III can be qualitatively reproduced. Therefore, it proves that the finding that an on average lower temperature can lead to faster precipitation is not a contradiction to the commonly assumed Arrhenius-type activation of a thermally activated process since precipitation is not taking place in thermal equilibrium here. The behaviour of excess vacancies in regimes I and II is of practical importance because the temperature and time ranges here are often used in industrial pre-ageing. Thus knowing these subtleties can help to predict or optimize heat treatment procedures.

4.4. Outlook

In this study, we have used a custom-made heating device to expose alloys to linear heating and demonstrated the benefit from a combination of five characterisation methods to extract more information about the precipitation process. This methodology could be extended to exploring more general non-isothermal treatments by modifying the controllers/programs and to bring temperature profiles closer to real industrial temperature profiles. A cooling unit (e.g. ventilator) could be added to achieve an even higher degree of freedom in temperature variations. Other characterisation methods could also be added, possibly after adapting sample geometries. The resulting experimental data could be used to validate the modelling of non-isothermal precipitation, especially data from in-situ experiments such as electrical resistivity, where a continuous dataset on one sample is measured.

5. Conclusions

We investigated clustering and precipitation during linear heating by using a custom-made heating device, which enables us to characterise the processes during heating in analogy to DSC on samples big enough to allow for in-situ electrical resistivity measurements and ex-situ positron lifetime measurements, in addition to conventionally applied hardness measurements and TEM. We focused primarily on low-temperature cluster formation, its impact on high temperature precipitation, and the influence of the heating rate. We find:

- Cluster formation during linear heating depends on the heating rate. Slower heating gives rise to more pronounced cluster formation.
- In an intermedite temperature range, linear heating to a given end temperature leads to stronger clustering than direct isothermal ageing at the end temperature for the same time.
- These two observations are expressed by the behaviour of excess vacancies as characterised by simulations. At lower temperatures, vacancies are more efficient in supporting solute diffusion and vacancy losses are relatively lower.
- Precipitation at higher temperatures is influenced by the clusters formed before as well as by the heating rate. For slower heating, a higher peak hardness is found associated with a higher precipitation fraction, finer and higher density of precipitates.
- An explicit cluster dissolution endotherm occurs only at high heating rate. It is proposed that the cluster dissolution signal at lower heating rate merges into the precipitation peak and causes the double peak structure in DSC trace.
- Cluster hardening is a linear function of heat released (i.e. to a good approximation precipitated solute fraction), whereas precipitate hardening (underage and peak-age) at higher temperatures follows the usual square root dependence on precipitated fraction. Cluster hardening per precipitated solute fraction is less efficient than precipitate hardening.

Acknowledgements

We thank Novelis R&D in Sierre for funding the research, providing the samples, and the fruitful discussions, in particular with Dr. Zeqin Liang and David Leyvraz. Work at Central South University was supported by the Open Research Fund (No. Kfkt2018-01) of the State Key Laboratory of High Performance Complex Manufacturing at the Central South University and National Natural Science Foundation of China (No. U2032117). We are thankful for the advice given by Prof. Wolfgang Pfeiler concerning the design of resistivity samples and to Norbert Beck for building the heating device.

References

[1] C. Haase, H. Wurst, Zur Frage der Kalt- und Warmaushärtung bei Aluminium-Magnesium-Silizium-Legierungen, Zeitschrift für Metallkunde 33 (1941) 399-403.
[2] C. Panseri, T. Federighi, A Resistometric Study of Preprecipitation in an Aluminium-1.4 Percent Mg2si Alloy, Journal of the Institute of Metals London 94 (1966) 99-197.
[3] I. Kovács, J. Lendvai, E. Nagy, The Mechanism of Clustering in Supersaturated Solid-Solutions of Al-Mg_2Si Alloys, Acta Metallurgica 20 (1972) 975-983.
[4] J. Banhart, M.D.H. Lay, C.S.T. Chang, A.J. Hill, Kinetics of natural aging in Al-Mg-Si alloys studied by positron annihilation lifetime spectroscopy, Physical Review B 83 (2011) 014101.
[5] S. Pogatscher, H. Antrekowitsch, H. Leitner, T. Ebner, P.J. Uggowitzer, Mechanisms controlling the artificial aging of Al-Mg-Si Alloys, Acta Materialia 59 (2011) 3352-3363.
[6] C.D. Marioara, S.J. Andersen, J. Jansen, H.W. Zandbergen, The influence of temperature and storage time at RT on nucleation of the beta " phase in a 6082 Al-Mg-Si alloy, Acta Materialia 51 (2003) 789-796.
[7] M.W. Zandbergen, Q. Xu, A. Cerezo, G.D.W. Smith, Study of precipitation in Al-Mg-Si alloys by atom probe tomography I. Microstructural changes as a function of ageing temperature, Acta Materialia 101 (2015) 136-148.
[8] X. Zhang, M. Liu, H. Sun, J. Banhart, Influence of Sn on the age hardening behavior of Al-Mg-Si alloys at different temperatures, Materialia 8 (2019) 100441.
[9] H.R. Shercliff, M.F. Ashby, A process model for age hardening of aluminium alloys - I. The model, Acta Metallurgica et Materialia 38 (1990) 1789-1802.
[10] O.R. Myhr, O. Grong, S.J. Andersen, Modelling of the age hardening behaviour of Al-Mg-Si alloys, Acta Materialia 49 (2001) 65-75.
[11] S. Esmaeili, D.J. Lloyd, W.J. Poole, A yield strength model for the Al-Mg-Si-Cu alloy AA6111, Acta Materialia 51 (2003) 2243-2257.
[12] D. Bardel, M. Perez, D. Nelias, A. Deschamps, C.R. Hutchinson, D. Maisonnette, T. Chaise, J. Gamier, F. Bourlier, Coupled precipitation and yield strength modelling for non-isothermal treatments of a 6061 aluminium alloy, Acta Materialia 62 (2014) 129-140.
[13] S.Q. Zhu, H.C. Shih, X.Y. Cui, C.Y. Yu, S.P. Ringer, Design of solute clustering during thermomechanical processing of AA6016 Al-Mg-Si alloy, Acta Materialia 203 (2021) 116455.
[14] D.W. Pashley, J.W. Rhodes, A. Sendorek, Delayed ageing in aluminium-magnesium-silicon alloys: effect on structure and mechnical properties, Journal of the Institute of Metals London 94 (1966) 41-49.
[15] J. Banhart, C.S.T. Chang, Z.Q. Liang, N. Wanderka, M.D.H. Lay, A.J. Hill, Natural Aging in Al-Mg-Si Alloys - A Process of Unexpected Complexity, Advanced Engineering Materials 12 (2010) 559-571.
[16] M.J. Starink, Analysis of aluminium based alloys by calorimetry: quantitative analysis of reactions and reaction kinetics, International Materials Reviews 49 (2004) 191-226.
[17] I. Dutta, S.M. Allen, A Calorimetric Study of Precipitation in Commercial Aluminum Alloy-6061, Journal of Materials Science Letters 10 (1991) 323-326.
[18] G.A. Edwards, K. Stiller, G.L. Dunlop, M.J. Couper, The precipitation sequence in Al-Mg-Si alloys, Acta Materialia 46 (1998) 3893-3904.
[19] C.S.T. Chang, J. Banhart, Low-Temperature Differential Scanning Calorimetry of an Al-Mg-Si Alloy, Metallurgical and Materials Transactions A 42A (2011) 1960-1964.
[20] Z. Yang, Z. Liang, D. Leyvraz, J. Banhart, Effect of pre-ageing on natural secondary ageing and paint-bake hardening in Al-Mg-Si alloys, Materialia 7 (2019) 100413.

[21] S. Esmaeili, D.J. Lloyd, Characterization of the evolution of the volume fraction of precipitates in aged AlMgSiCu alloys using DSC technique, Materials Characterization 55 (2005) 307-319.
[22] R. Ivanov, A. Deschamps, F. De Geuser, Clustering kinetics during natural ageing of Al-Cu based alloys with (Mg, Li) additions, Acta Materialia 157 (2018) 186-195.
[23] F. Lotter, D. Petschke, F. De Geuser, M. Elsayed, G. Sextl, T.E.M. Staab, In situ natural ageing of Al-Cu-(Mg) alloys: The effect of In and Sn on the very early stages of decomposition, Scripta Materialia 168 (2019) 104-117.
[24] M. Madanat, M. Liu, J. Banhart, Reversion of natural ageing in Al-Mg-Si alloys, Acta Materialia 159 (2018) 163-172.
[25] A. Serizawa, S. Hirosawa, T. Sato, Three-Dimensional Atom Probe Characterization of Nanoclusters Responsible for Multistep Aging Behavior of an Al-Mg-Si Alloy, Metallurgical and Materials Transactions A 39A (2008) 245-251.
[26] B. Milkereit, N. Wanderka, C. Schick, O. Kessler, Continuous cooling precipitation diagrams of Al-Mg-Si alloys, Materials Science and Engineering A 550 (2012) 87-96.
[27] B. Milkereit, M.J. Starink, Quench sensitivity of Al-Mg-Si alloys: A model for linear cooling and strengthening, Materials & Design 76 (2015) 117-129.
[28] S. Esmaeili, W.J. Poole, D.J. Lloyd, Study of the kinetics of precipitation during artificial aging of Al-Mg-Si(-Cu) alloys using isothermal calorimetry method, Aluminum 2003 (2003) 177-185.
[29] B. Milkereit, L. Giersberg, O. Kessler, C. Schick, Isothermal Time-Temperature-Precipitation Diagram for an Aluminum Alloy 6005A by In Situ DSC Experiments, Materials 7 (2014) 2631-2649.
[30] W.F. Miao, D.E. Laughlin, A differential scanning calorimetry study of aluminum alloy 6111 with different pre-aging treatments, Journal of Materials Science Letters 19 (2000) 201-203.
[31] A.K. Gupta, D.J. Lloyd, S.A. Court, Precipitation hardening processes in an Al-0.40%Mg-1.3%Si-0.25%Fe aluminum alloy, Materials Science and Engineering A 301 (2001) 140-146.
[32] D.J. Lloyd, D.R. Evans, A.K. Gupta, Precipitation reactions and the differential scanning calorimetry response of AA6111 alloy, Canadian Metallurgical Quarterly 39 (2000) 475-481.
[33] F. De Geuser, B. Gault, Metrology of small particles and solute clusters by atom probe tomography, Acta Materialia 188 (2020) 406-415.
[34] Z. Yang, J. Banhart, Natural and artificial ageing in aluminium alloys – the role of excess vacancies, Acta Materialia 215 (2021) 117014.
[35] M. Liu. Clustering kinetics in Al-Mg-Si alloys investigated by positron annihilation techniques, PhD thesis. Berlin: Technische Universität Berlin, 2014.
[36] S.J. Andersen, H.W. Zandbergen, J. Jansen, C. Traeholt, U. Tundal, O. Reiso, The crystal structure of the ß" phase in Al-Mg-Si alloys, Acta Materialia 46 (1998) 3283-3298.
[37] Z. Matyas, Change of electrical resistance of alloys during ageing, Philosophical Magazine 40 (1949) 324-337.
[38] H. Herman, J.B. Cohen, Resistivity changes due to formation of G. P. Zones, Nature 191 (1961) 63-64.
[39] C.D. Marioara, S.J. Andersen, H.W. Zandbergen, R. Holmestad, The influence of alloy composition on precipitates of the Al-Mg-Si system, Metallurgical and Materials Transactions A 36A (2005) 691-702.
[40] S.J. Andersen, Quantification of the Mg2Si ß" and ß' Phases in AlMgSi Alloys by Transmission Electron Microscopy, Metallurgical and Materials Transaction A 26A (1995) 1931-1937.

[41] P.H. Ninive, A. Strandlie, S. Gulbrandsen-Dahl, W. Lefebvre, C.D. Marioara, S.J. Andersen, J. Friis, R. Holmestad, O.M. Lovvik, Detailed atomistic insight into the beta" phase in Al-Mg-Si alloys, Acta Materialia 69 (2014) 126-134.
[42] S. Esmaeili, D.J. Lloyd, W.J. Poole, Effect of natural aging on the resistivity evolution during artificial aging of the aluminum alloy AA6111, Materials Letters 59 (2005) 575-577.
[43] T.E.M. Staab, R. Krause-Rehberg, U. Hornauer, E. Zschech, Study of artificial aging in AlMgSi (6061) and AlMgSiCu (6013) alloys by positron annihilation, Journal of Materials Science 41 (2006) 1059-1066.
[44] M. Madanat, M. Liu, X. Zhang, Q. Guo, J. Cizek, J. Banhart, Co-evolution of vacancies and solute clusters during artificial ageing of Al-M-Si alloys, Physical Review Materials 4 (2020) 063608.
[45] L. Resch, G. Klinser, E. Hengge, R. Enzinger, M. Luckabauer, W. Sprengel, R. Würschum, Precipitation processes in Al-Mg-Si extending down to initial clustering revealed by the complementary techniques of positron lifetime spectroscopy and dilatometry, Journal of Materials Science 53 (2018) 14657-14665.
[46] S.N. Kim, E. Kobayashi, T. Sato, Formation behavior of nanoclusters in Al-Mg-Si alloys with different Mg and Si composition, Materials Science Forum 794-796 (2014) 957-962.
[47] V.A. Esin, L. Briez, M. Sennour, A. Köster, E. Gratiot, J. Crepin, Precipitation-hardness map for Al-Cu-Mg alloy (AA2024-T3), Journal of Alloys and Compounds 854 (2021) 157164.
[48] M. Song, B. Liao, A modulated DSC characterization of morphology of composite latex particles, Thermochimica Acta 423 (2004) 57-61.
[49] B. Schäffer, B. Schäffer, D. Lörinczy, Decomposition of DSC curves of dairy products with Gaussian functions, Journal of Thermal Analysis and Calorimetry 82 (2005) 531-535.
[50] M. Elsabee, R.J. Prankerd, Solid-state properties of drugs. II. Peak shape analysis and deconvolution of overlapping endotherms in differential scanning calorimetry of chiral mixtures, International Journal of Pharmaceutics 86 (1989) 211-219.
[51] M. Mantina, Y. Wang, L.Q. Chen, Z.K. Liu, C. Wolverton, First principles impurity diffusion coefficients, Acta Materialia 57 (2009) 4102-4108.
[52] M.J. Starink, L.F. Cao, P.A. Rometsch, A model for the thermodynamics of and strengthening due to co-clusters in Al-Mg-Si-based alloys, Acta Materialia 60 (2012) 4194-4207.
[53] S. Pogatscher, H. Antrekowitsch, P.J. Uggowitzer, Influence of starting temperature on differential scanning calorimetry measurements of an Al-Mg-Si alloy, Materials Letters 100 (2013) 163-165.
[54] C.H. Liu, Y.X. Lai, J.H. Chen, G.H. Tao, L.M. Liu, P.P. Ma, C.L. Wu, Natural-aging-induced reversal of the precipitation pathways in an Al–Mg–Si alloy, Scripta Materialia 115 (2016) 150-154.

Figures

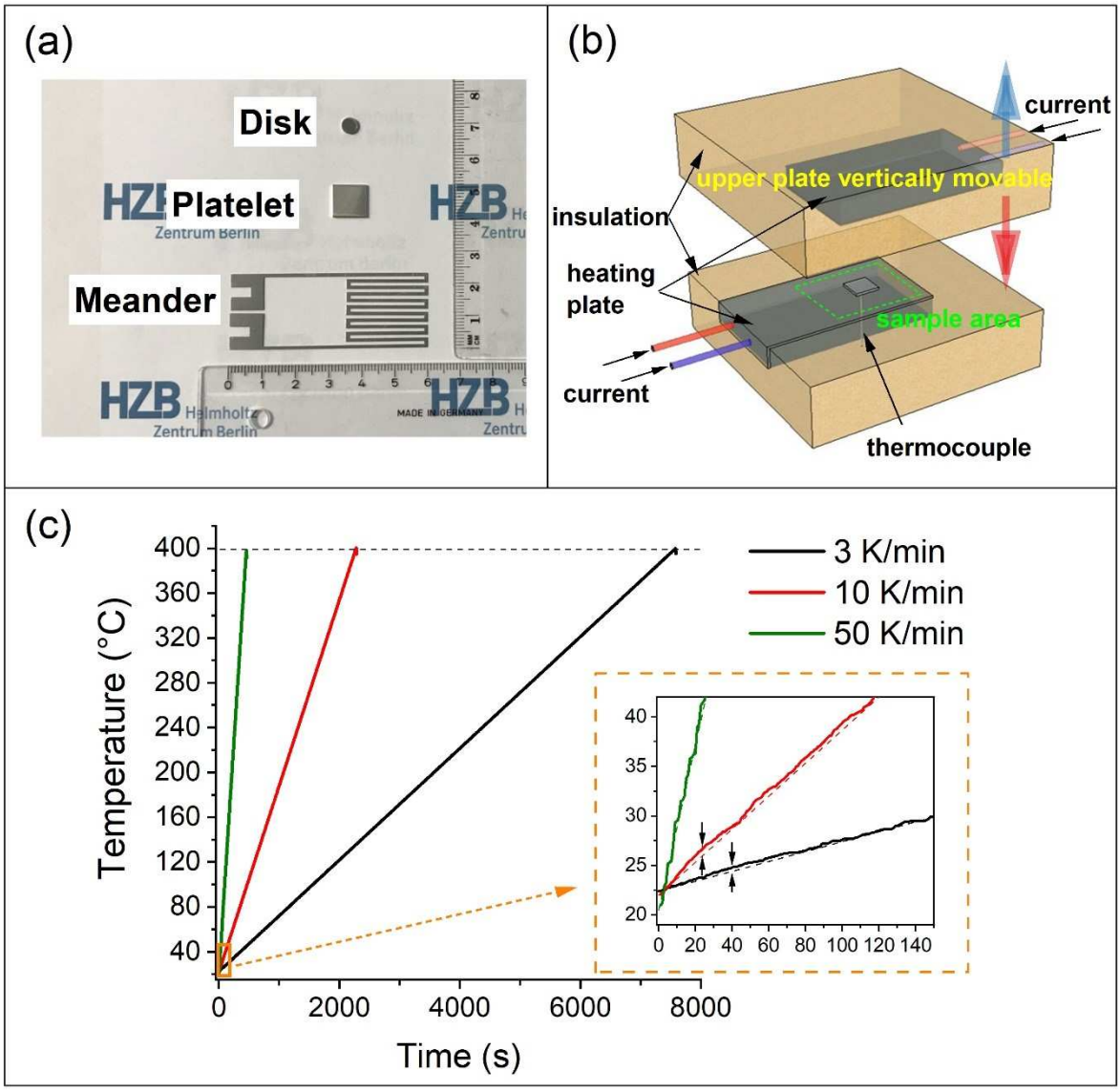

Fig. 1. (a) Various sample geometries used in the experiments. *Disk*: DSC measurement. *Platelet*: hardness measurement and PALS. *Meander*: electrical resistivity measurement. (b) Schematic of heating device. (c) Experimental heating curves from room temperature ~20 °C to 400 °C. Inset: zoom-in of the initial temperature overshoots (arrows) deviating from perfect linear heating (broken lines) The axis labels and units for the inset are the same as for the main Fig. 1c.

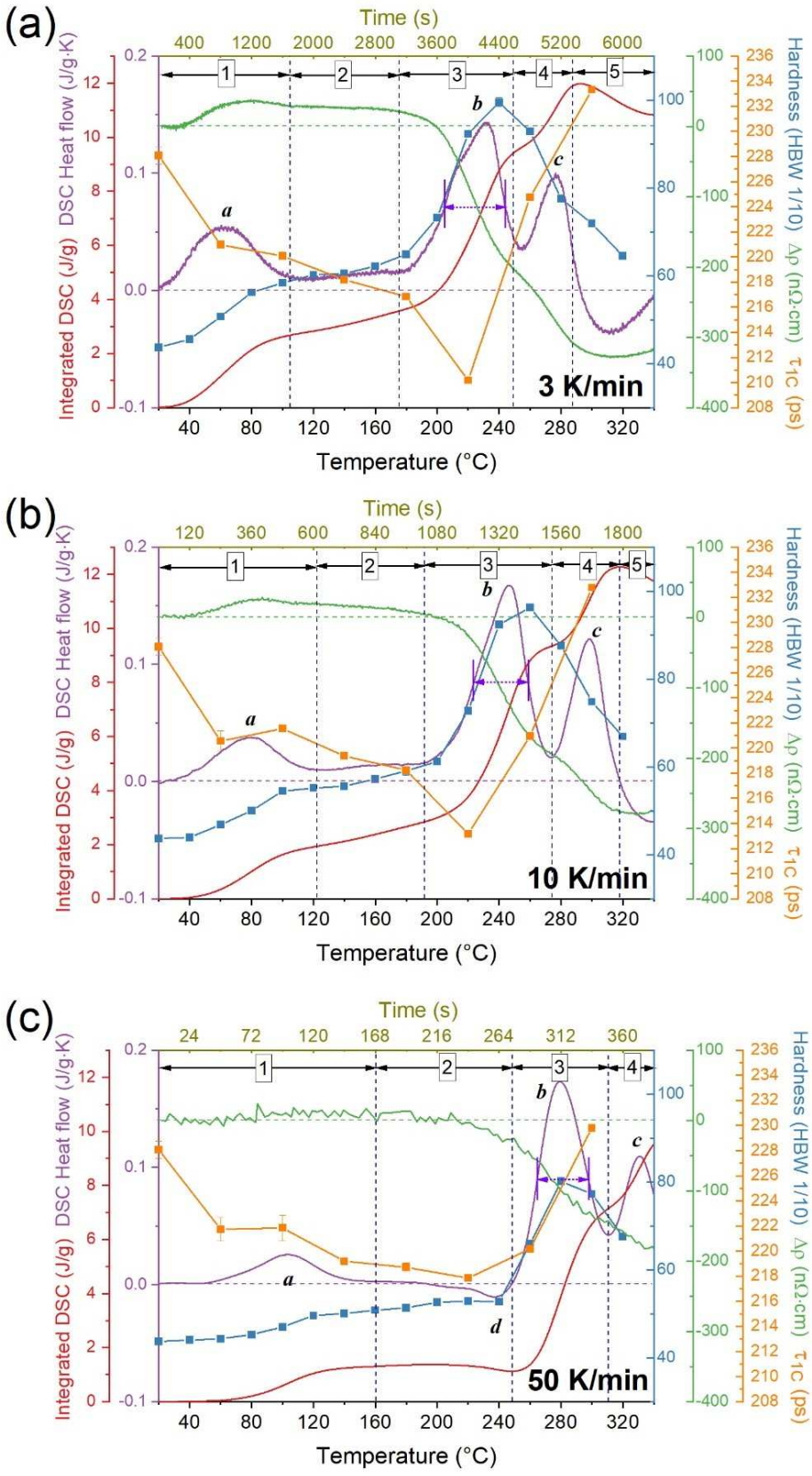
(a)
Time (s)
400 1200 2000 2800 3600 4400 5200 6000
1 2 3 4 5
a
b
c
3 K/min
Integrated DSC (J/g)
DSC Heat flow (J/g·K)
Hardness (HBW 1/10)
Δρ (nΩ·cm)
τ1C (ps)
Temperature (°C)
(b)
Time (s)
120 360 600 840 1080 1320 1560 1800
1 2 3 4 5
a
b
c
10 K/min
Integrated DSC (J/g)
DSC Heat flow (J/g·K)
Hardness (HBW 1/10)
Δρ (nΩ·cm)
τ1C (ps)
Temperature (°C)
(c)
Time (s)
24 72 120 168 216 264 312 360
1 2 3 4
a
b
c
d
50 K/min
Integrated DSC (J/g)
DSC Heat flow (J/g·K)
Hardness (HBW 1/10)
Δρ (nΩ·cm)
τ1C (ps)
Temperature (°C)

Fig. 2. Evolution of various properties during linear heating at (a) 3 $K \cdot min^{-1}$ (b) 10 $K \cdot min^{-1}$, (c) 50 $K \cdot min^{-1}$, all after solutionising and quenching. Precipitation stages are defined by vertical broken lines and numbered. Horizontal dotted lines represent the zero values of two of the observables. Different DSC peaks are denoted by letters *a*–*c*. Data delimited by the purple dotted line in stage 3 are further investigated in Fig. 5b.

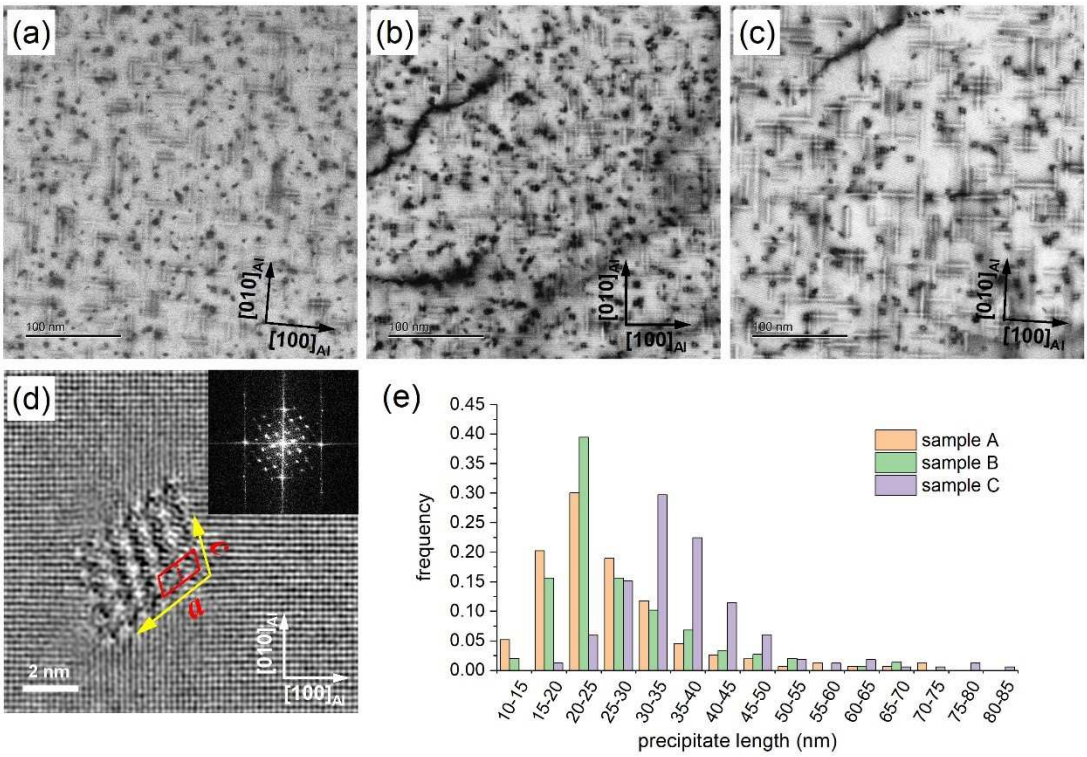

Fig. 3. (a – c) BF images of samples after linear heating to peak hardness, (a) 240 °C at 3 K·min^{-1} (sample A), (b) 260 °C at 10 K·min^{-1} (sample B), and (c) 280 °C at 50 K·min^{-1} (sample C). (d) Representative HAADF image of a needle-shaped precipitate viewed along the needle axis. Red box marks the unit cell of the β″ structure. The lattice parameters *a* and *c* are measured after calibrating the drift distortion using the known Al lattice constant. Yellow arrows indicate the orientation relationships between the precipitate and the Al matrix. Inset shows the fast Fourier transform of the image. (e) Precipitate length distribution based on a statistics of ~150 precipitates in the three samples appearing in (a – c).

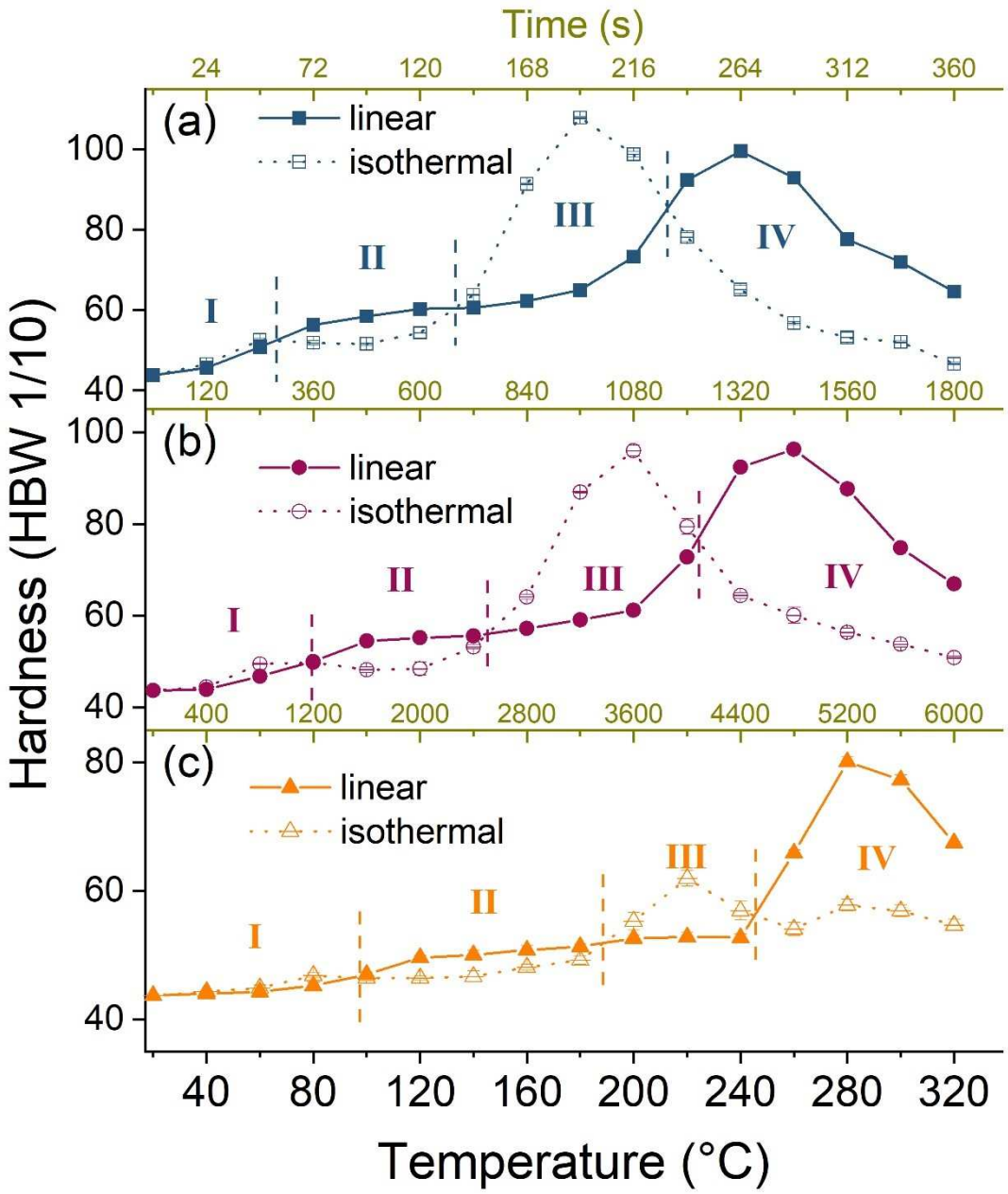

Fig. 4. Comparison of hardening caused by isothermal ageing and linear heating at (a) 3 K·min^{-1}, (b) 10 K·min^{-1}, (c) 50 K·min^{-1}. The isothermal ageing time was the same as the heating time to a given temperature, namely $t = \frac{T-20°C}{\phi}$. Note that the 'isothermal ageing' curve does not represent a continuous heat treatment but a connection of individual hardnesses after isothermal ageing at various temperatures for various times.

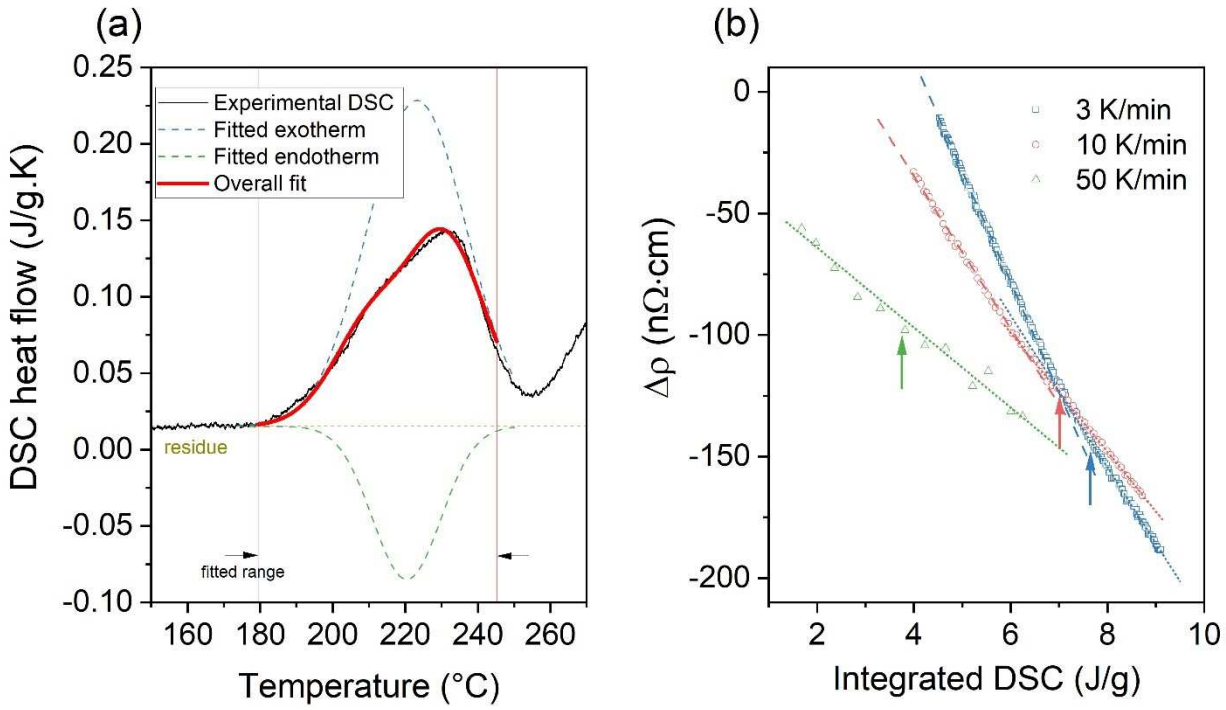

Fig. 5. (a) Fitting of peak *b* in the DSC trace of 3 K·min^{-1} (Fig. 2a) using one positive and one negative Gaussian function. (b) Electrical resistivity change as a function of DSC integral at the peak *b*. Data taken from the marked ranges in Fig. 2. Arrows point at the positions of the peak *b*. Dashed and dotted lines represent the two stages. For 50 K·min^{-1}, due to fluctuations of the resistivity data it is hard to determine two stages.

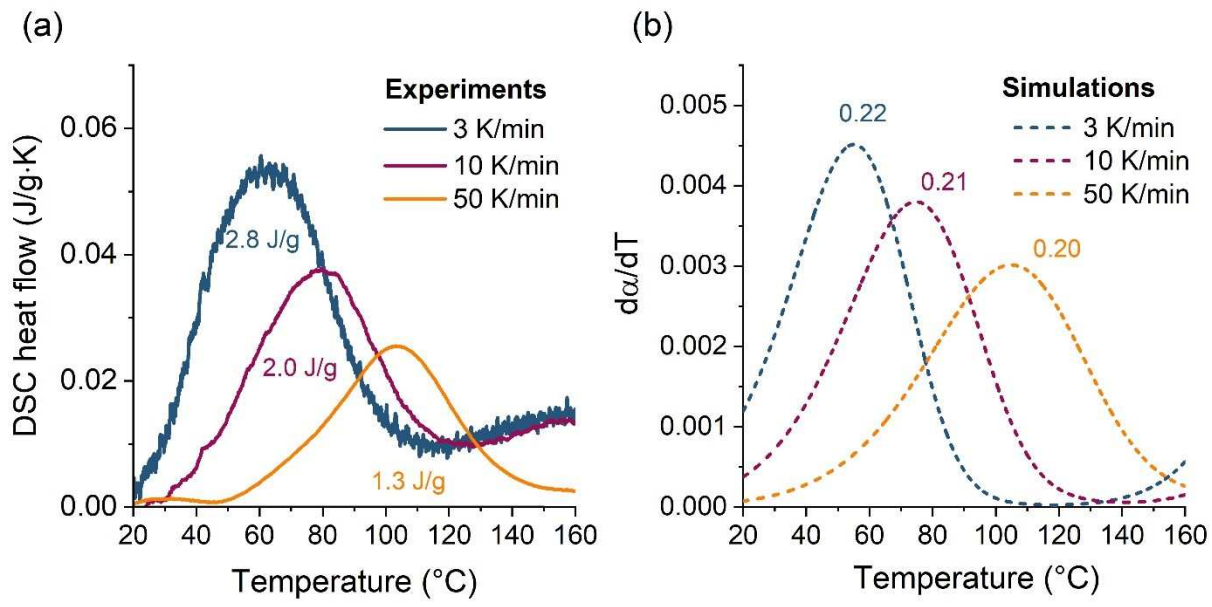

Fig. 6. Experimental DSC cluster peaks (a) and simulated cluster peaks in linear heating (b) using the model and parameters developed in Ref. [34]. Values below the peaks in (a) and beside the peaks in (b) denote the integrated peak areas.

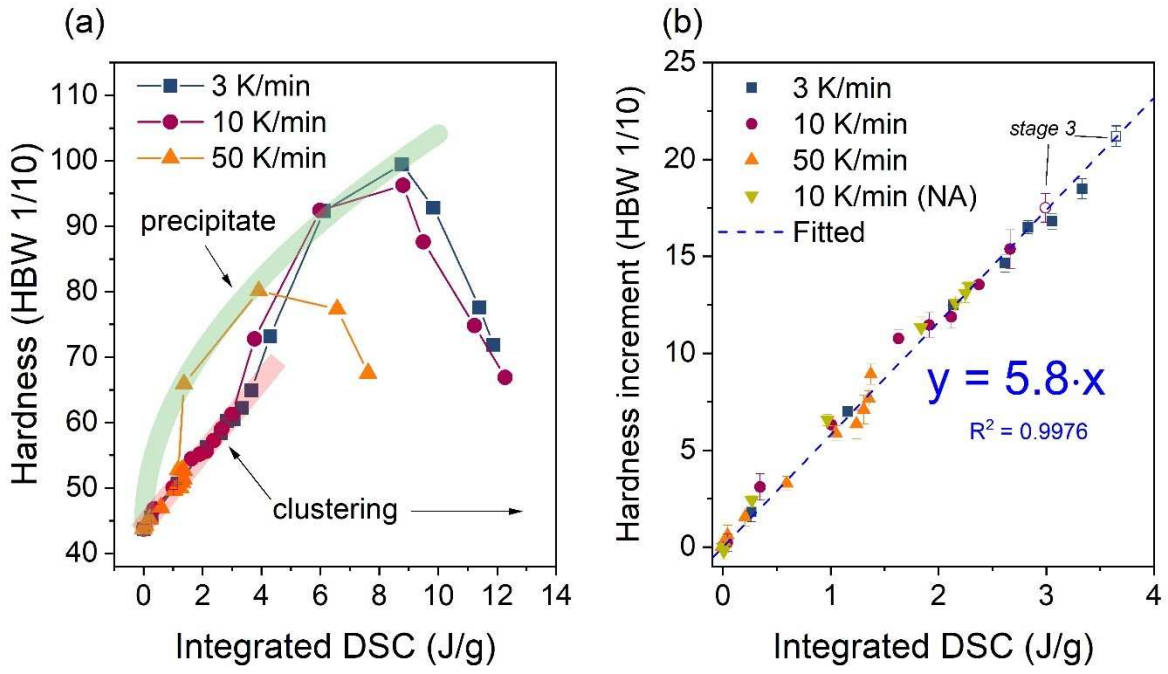

Fig. 7. (a) Hardness plotted as a function of DSC integral for various heating rates. The red-shaded region is further replotted in (b) where the hardness increment relative to the state before linear heating is presented, featuring a linear relationship $\Delta\mathcal{H} \propto Q_{int}$. The green-shaded area in (a) represents a square root relationship $\Delta\mathcal{H} \propto \sqrt{Q_{int}}$. (b) also includes data of cluster hardening during linear heating at 10 K·min^{-1} of samples after natural ageing (NA) for 1 h (supplement Fig. S5).

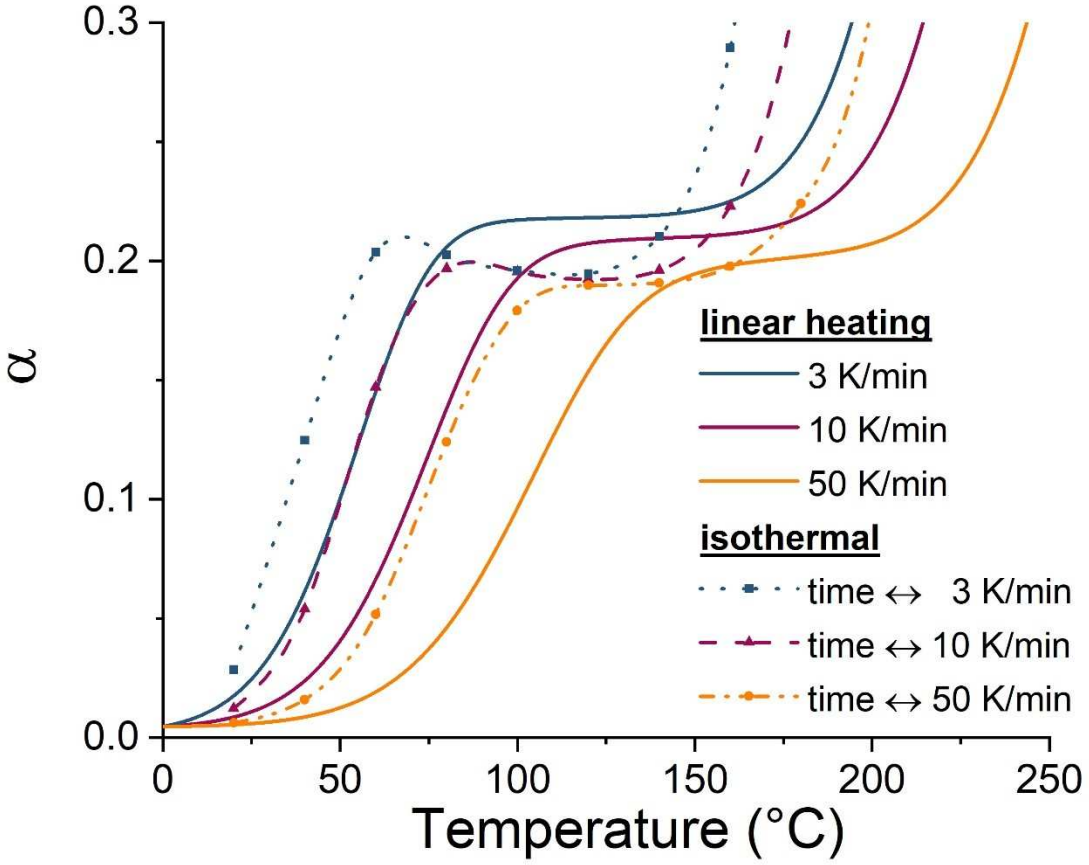

Fig. 8. Representation of the phenomena occurring in Fig. 4 using the model and parameters in Ref. [34] to explain the role of excess vacancies during ageing. "Isothermal" at temperature T refers to ageing for a time $t = \frac{T-20°C}{\phi}$, corresponding to given reference heating rate ϕ.

Supplementary Material

S1. Device for linear heating

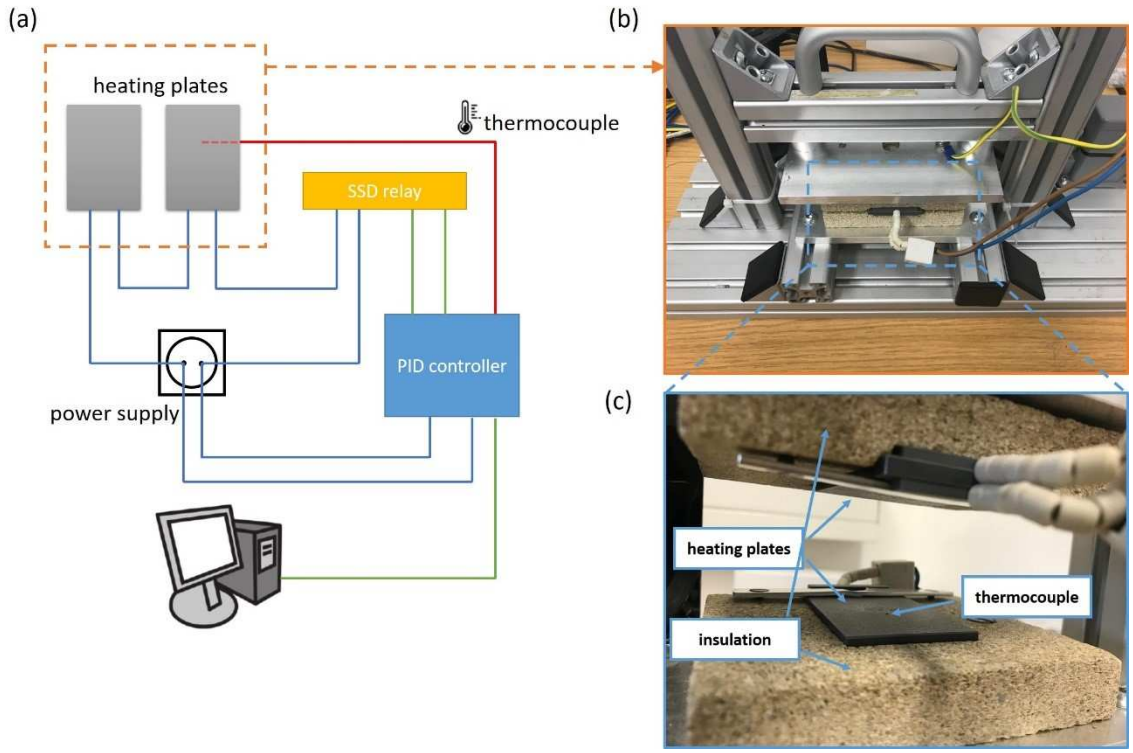

Fig. S1. (a) Schematic circuit diagram of the heating device. (b, c) Photos of the heating device.

S2. Comparison of DSC from different starting temperatures

Ideally the heating in all characterised samples should start from the same temperature so that dif. As mentioned in Sec. 2.2 of the main paper, DSC was started from a lower temperature than in other techniques, e.g. resistivity measurement, where heating was performed from room temperature (20 ± 2 °C). The reason for this was to avoid the influence of initial instabilities of the DSC device on the signal. An example is shown in Fig. S2, where it is seen that the initial instability of the DSC signal

has merged into the first peak when DSC is started from 20 °C. The question arising from this treatment is whether the DSC peaks of interest will be influenced the period. Fig. S2 shows the influence of starting temperature on the DSC traces of 3 K·min^{-1}, which suffers from the longest time below 20 °C. It is shown that the peaks are not much influenced except for very high temperature regime, which could be due to the baseline drift, but such high temperature regime is not of our interest anyway.

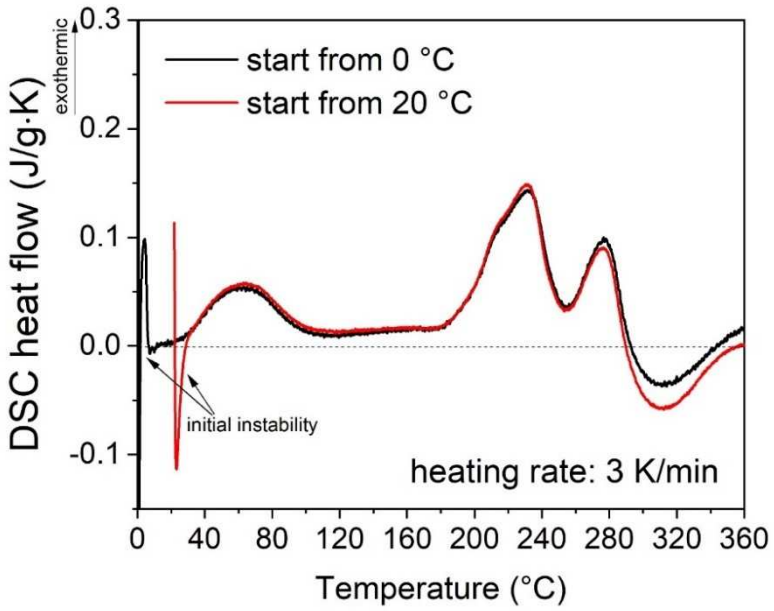

Fig. S2. DSC curves of 3 K·min^{-1} started from 0 °C and 20 °C.

S3. Electrical resistivity data processing

Four-point probe electrical resistivity is measured normally using the Eq. (S1)

$$\rho = \frac{U \times A}{I \times L} \tag{S1}$$

where U is the measured voltage, A is the cross-section area, I is the measured electric current, and L is the length. Due to the variation in sample preparation, A and L are not the same for all the samples, thus the measured ρ and its change $\Delta\rho$ during precipitation processes are not always comparable for different samples, especially for quantitative analysis. To overcome this, we presume the resistivity of

the quenched alloy at 20 °C a constant value $\rho_{AQ}(20\ °C) = 3911\ n\Omega\ cm$, which we have measured in the previous publication [1] and applied the first correction in Eq. (1) in the main paper.

This correction is successful as can be seen in Fig. S3(a, b) that the resistivity measured during reheating at various heating rates (where the precipitation is small) are almost identical after correction.

Subsequently, the phonon contribution to the resistivity needs to be subtracted as we are interested only in the precipitation related resistivity change. This is done by linearly fitting the curves in Fig. S3(b) in the range of 20 – 310 °C and a temperature coefficient ρ' obtained. The final resistivity change relative to the resistivity at 20 °C is calculated using Eq. (2) in the main paper.

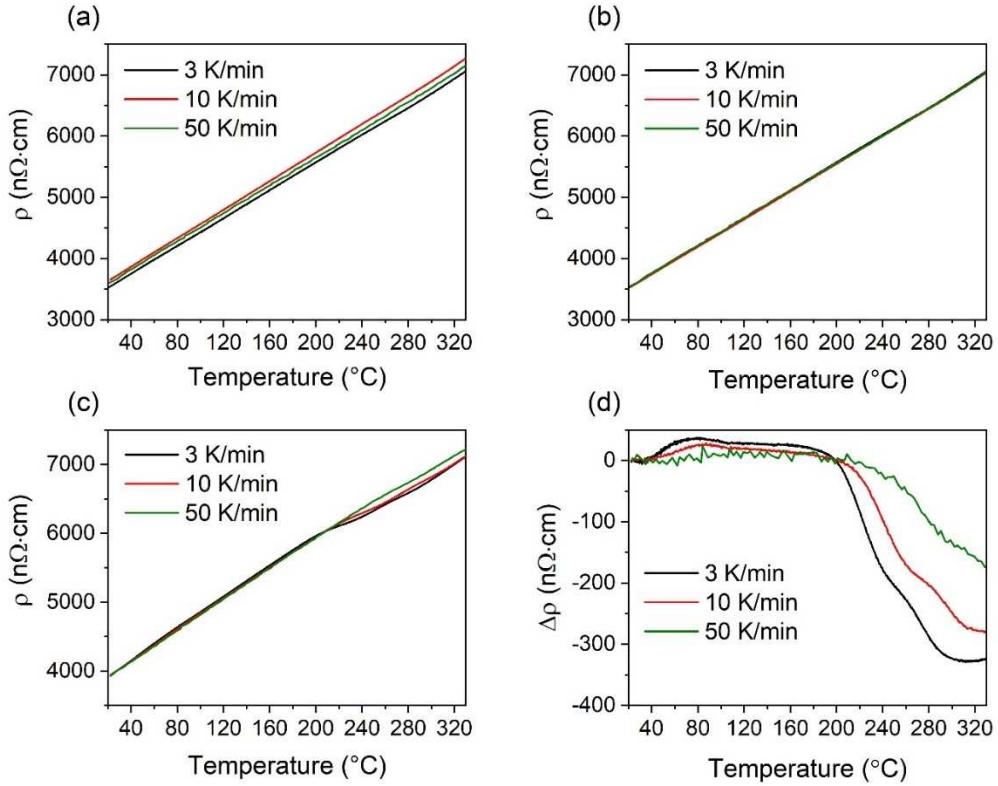

Fig. S3. (a–b) Electrical resistivity measured during the reheating calculated using Eq. (S1) (a) and Eq. (S2) (b). (c) Electrical resistivity of AQ sample during initial run after correction using Eq. (S2).

(d) Electrical resistivity change due to precipitation during heating of AQ sample after correction of phonon contribution using Eq. (S3).

S4. PALS data during natural ageing

Positron lifetime measurements were performed ex-situ at room temperature. Since the microstructure might further evolve during natural secondary ageing (NSA), it is important to first evaluate the influence of the NSA on the positron lifetimes. If the evolution of positron lifetime during NSA is not pronounced, we could collect more spectra (longer time) during NSA to ensure a more accurate positron lifetime analysis, and if positron lifetime evolves fast during NSA, then only the lifetime spectra in the very initial NSA should be taken for analysis with a larger inaccuracy. Therefore we first combine the lifetime spectra during NSA with a small time interval of four minutes (~2×10^5 counts) to obtain a time-dependent one-component positron lifetime analysis, as presented in Fig. S4 (a-c). It is seen that the positron lifetime for the most samples are fluctuating around a central value in the initial NSA (fluctuation and error bar due to the small counts), except for samples after short treatments such as 60_50, 100_50 and 60_10 (first digit stands for the end temperature of heating and the second for the heating rate), where τ_{1C} appears to be increasing in the first hour of NSA. Thus, for these samples only the first data points during NSA (time interval of 4 min) were used, and for other samples a longer spectra collection time of 1 h (~2×10^6 counts) was applied and a small error bar obtained for the lifetimes (Fig. S4d).

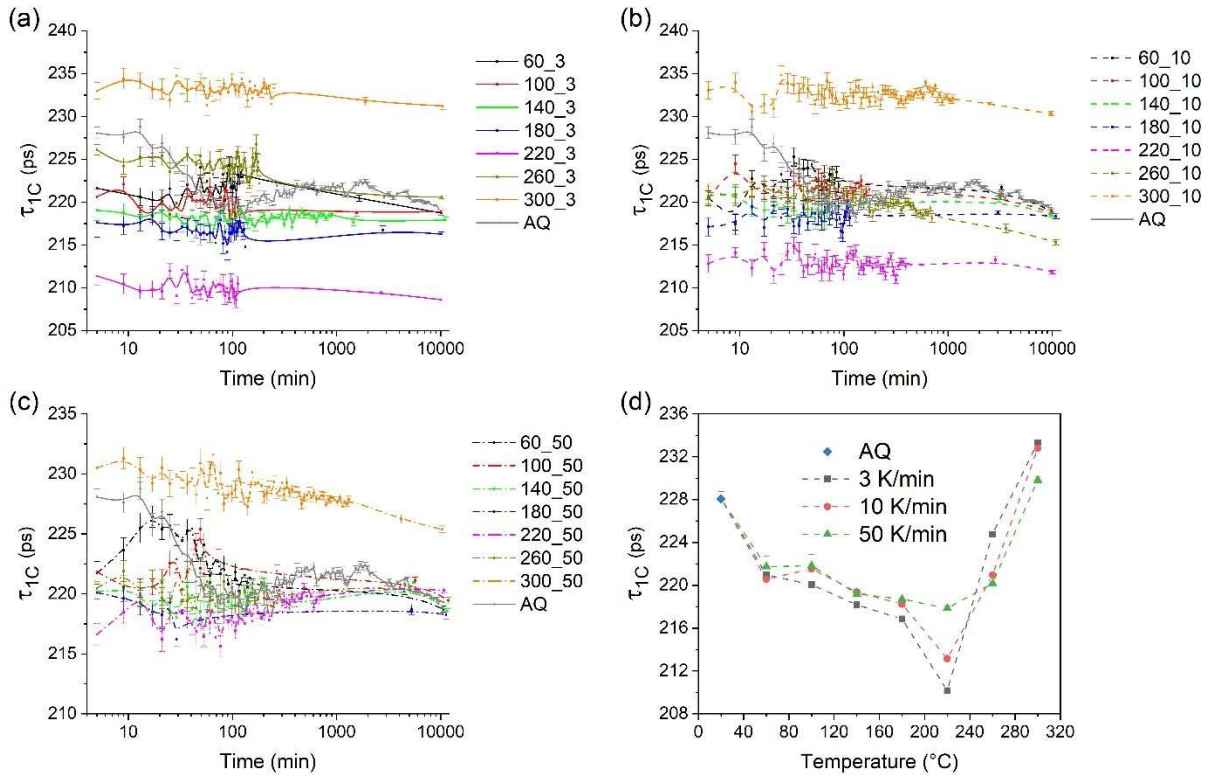

Fig. S4. One-component positron lifetime τ_{1C} as a function of NSA time after linear heating at various heating rates: (a) 3 K·min^{-1}, (b) 10 K·min^{-1}, (c) 50 K·min^{-1}.

S5. Linear heating of naturally aged sample

Fig. S5 presents DSC traces as well as the hardness evolution during linear heating of naturally aged samples (NA 1 h). A strong clustering peak is observed, which is accompanied by a hardness increase. These data are used in main paper Fig. 8b. A pronounced endothermic trough at ~220 °C is observed, pointing at the dissolution of clusters formed during NA and during linear heating. Hardness correspondingly decreases due to reversion of the clusters formed before the DSC run. Such reversion also takes place without this additional natural ageing, but the effect is less pronounced as no decrease of hardness is observed but just a change of the rate of increase (Figs. 2–4 of the main paper).

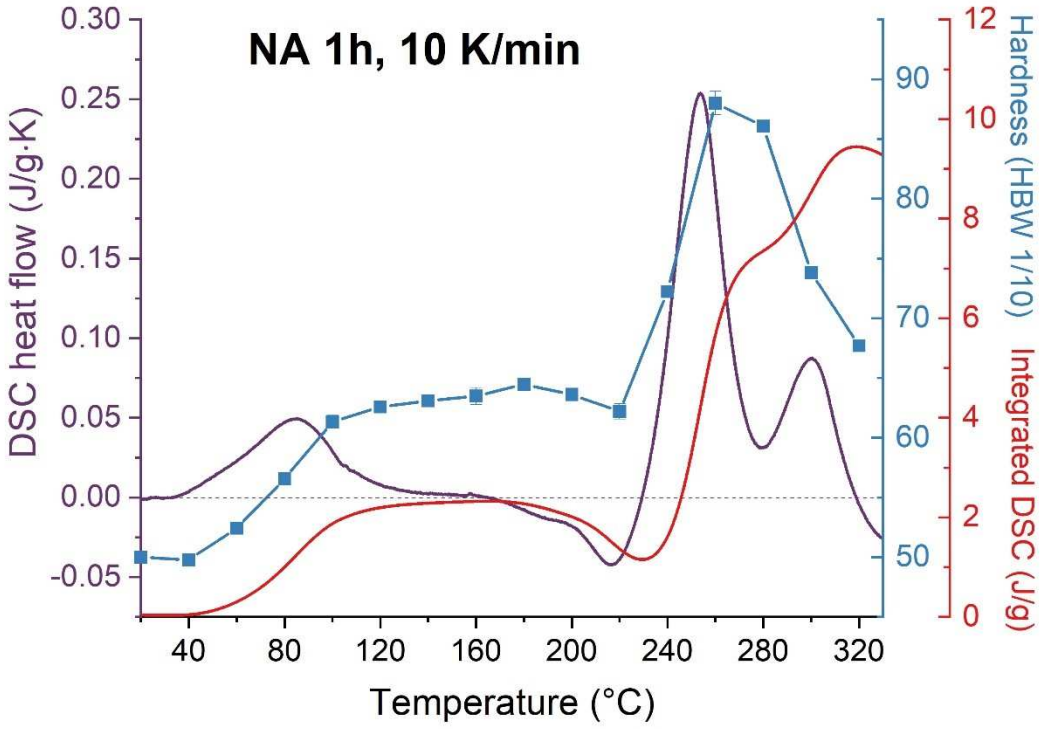

Fig. S5. Evolution of DSC trace, integrated DSC, and hardness during heating at 10 K·min^{-1} for samples naturally aged for 1 h.

S6. Comparison of linear heating and isothermal ageing in Al-0.6Mg-0.8Si alloy

In the main text Sec. 3.3 it is shown in 6014 alloy (slightly richer in Mg) that linear heating can lead to stronger hardening than isothermal ageing for equal time. Similar result has also been observed in another Si-richer alloy (Al-0.6Mg-0.8Si), which contains 0.6% Mg and 0.8% Si (all in wt.) [2]. The data have been extracted and replotted in the following Fig. S6, where it is seen that linear heating to the intermediate temperature range (~100 °C) results in higher hardness than isothermal ageing at that end temperature for the same time.

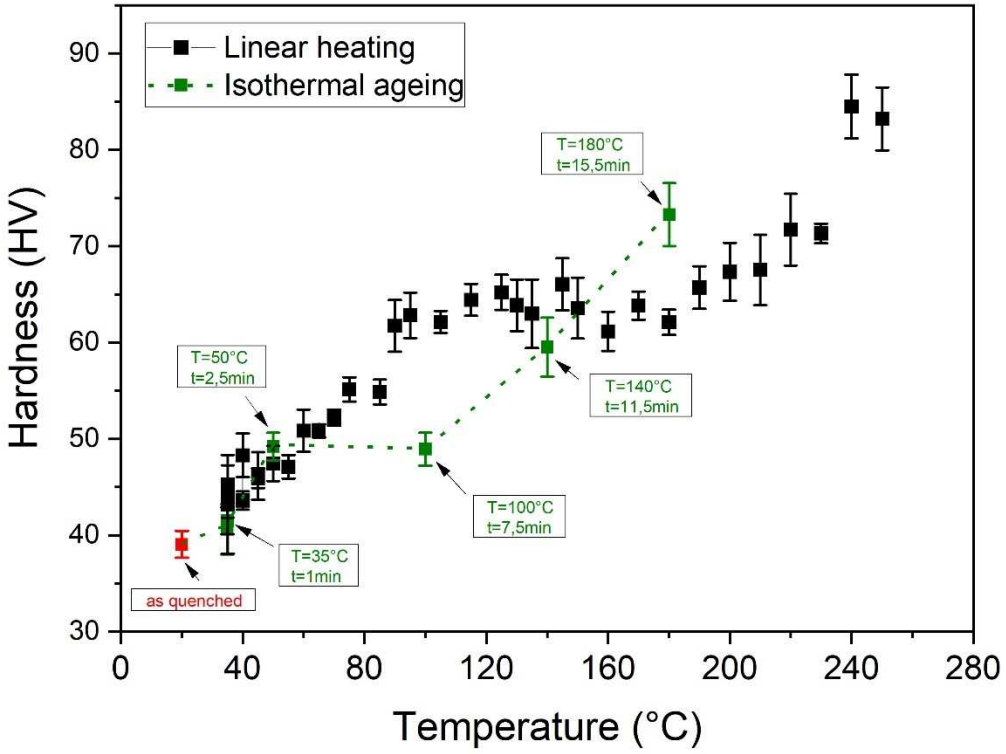

Fig. S6. Comparison of hardnesses after linear heating and isothermal ageing for equal times in alloy Al-0.6Mg-0.8Si [2].

References

[1] Z. Yang, Z. Liang, D. Leyvraz, J. Banhart, Effect of pre-ageing on natural secondary ageing and paint-bake hardening in Al-Mg-Si alloys, Materialia 7 (2019) 100413.
[2] A. Röhsler, Untersuchung des Einflusses der Kaltauslagerung auf die Warmauslagerung in Al-Mg-Si-Legierungen, Diplom Thesis, TU Bergakademie Freiberg (2015).